

Three-layer photocarrier radiometry model of ion-implanted silicon wafers

Bincheng Li,^{a)} Derrick Shaughnessy, Andreas Mandelis,^{b)} and Jerias Batista^{c)}

Center for Advanced Diffusion-Wave Technologies (CADIFT), Department of Mechanical and Industrial Engineering, University of Toronto, Toronto, ON, M5S 3G8, Canada

Jose Garcia

Photo-Thermal Diagnostics, Inc., 232 College St., Toronto, ON, M5T 1R5, Canada

(Received 15 December 2003; accepted 23 March 2004)

A three-dimensional three-layer model is presented for the quantitative understanding of the infrared photocarrier radiometry (PCR) response of ion-implanted semiconductors, specifically Si. In addition to the implanted layer and intact substrate normally assumed in all existing two-layer theoretical models to describe the photothermal response of ion-implanted semiconductors, a surface layer is considered in this three-layer model to represent a thin, less severely damaged region close to the surface. The effects on the PCR signal of several structural, transport, and optical properties of ion-implanted silicon wafers affected significantly by the ion implantation process (minority carrier lifetime, diffusion coefficient, optical absorption coefficient, thickness of the implanted layer, and front surface recombination velocity) are discussed. The dependence of the PCR signal on the ion implantation dose is theoretically calculated and compared to experimental results. Good agreement between experimental data and theoretical calculations is obtained. Both theoretical and experimental results show the PCR dependence on dose can be separated into four regions with the transition across each region defined by the implantation-induced electrical and optical degrees of damage, respectively, as the electrical and optical damage occurs at different dose ranges. It is also shown that the PCR amplitude decreases monotonically with increasing implantation dose. This monotonic dependence provides the potential of the PCR technique for industrial applications in semiconductor metrology. © 2004 American Institute of Physics. [DOI: 10.1063/1.1748862]

I. INTRODUCTION

Ion implantation is a key technological process for surface modification of semiconductor materials during microelectronic manufacturing. Control of the accuracy and uniformity of the ion implantation dose is critical to normal device performance and wafer yield. To fulfill such a high-accuracy control, highly sensitive and reliable metrological methods are required. Ion beam techniques such as secondary ion mass spectrometry (SIMS) and Rutherford backscattering (RBS) are capable of generating depth profiles of dopants before or after electrical activation.¹ Density profiles of electrically activated dopants can also be generated using spreading resistance profiling (SRP).² However, each of these techniques has drawbacks that limit their application to industrial process monitoring. RBS is limited to detecting ions that are massive relative to the substrate atoms. SIMS is by nature a destructive technique and SRP is a destructive technique requiring complex sample preparation. For industrial dose and uniformity monitoring a complete and detailed reconstruction of the implant layer is not required and fac-

tors such as time, resolution, sensitivity, required processing, and the destructive or nondestructive nature of the process have varying degrees of importance. Monitoring industrial implantation processes does not require detailed depth profiles of the implants since uniformity over the wafer and reproducibility are the two factors that most directly affect device yield and reliability. The four-point probe sheet resistance technique³ is commonly used in industrial monitoring of dose and uniformity. The main drawbacks of this technique are the limited resolution due to size of the probes, the damage resulting from contact with the sample, and the long delay between the process and measurement due to the required annealing process to activate the ions. Optical approaches including optical densitometry⁴ and photothermal techniques^{5–11} offer an alternative that addresses these limitations of the four point probe technique by using beam sizes on the order of microns to monitor the degree of damage to a substrate immediately following the implantation process in a completely noncontact, nondestructive manner.

In the past decades, photothermal methods, mainly photomodulated thermoreflectance (PMR)^{5–8} and photothermal radiometry (PTR),^{9–11} have been proven to be powerful tools for dose monitoring and uniformity mapping. Most recently, photocarrier radiometry (PCR)^{12,13} was introduced and found to be a sensitive method for characterization, depth profiling, and subsurface defect imaging of semiconductor materials. It has also recently been used for ion implantation dose monitoring.¹⁴ In contrast to PMR and PTR, PCR is a purely

^{a)}Also affiliated with Photo-Thermal Diagnostics, Inc., 232 College St., Toronto, ON, M5T 1R5, Canada.

^{b)}Also affiliated with Photo-Thermal Diagnostics, Inc., 232 College St., Toronto, ON, M5T 1R5, Canada.

^{c)}On leave from Departamento de Física, Universidade Federal do Maranhão; Av. dos Portugueses, s/n, 65085-580 São Luis, MA, Brazil; electronic mail: jbatista@ufma.br

carrier-wave laser-based detection methodology, which is most sensitive to the electrical transport parameters of semiconductor materials. It has been shown that the PCR signal amplitude has a monotonic dependence on the implantation dose over a wide range of species, implantation dose, and energy.¹⁴ This is a very important advantage over PMR and PTR for industrial applications as the dose could be determined through a simple calibration procedure.

Even though the monotonic dependence of the PCR signal on implantation dose greatly simplifies the dose monitoring, the quantitative understanding of this monotonic dependence is a difficult task due to the complicated physical nature of the optoelectronic response from ion-implanted semiconductors: therefore a complete theoretical description does not exist. There have been several theoretical models for the photothermal response of ion-implanted semiconductors, developed for both PMR and PTR in the past two decades. Wurm *et al.*¹⁵ developed a one-dimensional (1D) model for PMR, in which only the free-carrier-wave component was taken into account. Christofides *et al.*¹⁶ developed a 1-D PMR model considering both plasma- and thermal-effects, while Liu *et al.*¹⁷ developed a complete 3D model in which the finite size of the excitation beam was taken into account. All three of these PMR models are two-layer models that treat the ion-implanted region in the semiconductor as a single layer with uniform properties (The second layer is the remaining intact substrate). On the other hand, recently Salnick and Opsal^{18,19} developed a multilayer model to calculate quantitatively the photothermal response of a spatially inhomogeneous ion-implanted semiconductor. For PTR, Nestoros *et al.*²⁰ developed a 1D two-layer model, while Salnick and Mandelis²¹ and Salnick *et al.*²² reported theoretical and experimental depth profiling of ion-implanted wafers treated as an electrically inhomogeneous medium.

A common disadvantage of all two-layer models is that the structure of the ion-implanted layer is over-simplified; in fact the implanted layer has nonuniform properties. The multilayer models much better represent the real structure of the implanted layer. The disadvantages of the multilayer models are that theoretically they are complicated, and computationally the values of many parameters involved in the models are actually not known. This gives rise to concerns about the uniqueness issue which is yet to be addressed. A compromise between the simplicity of the two-layer models and the complexity of the multilayer models is the development of a three-layer model. For ion-implanted semiconductors, a three-layer structure, while avoiding the complication of the multilayer model, better represents the real situation than the simple two-layer model, because the ions do not reside within a thin layer very close to the surface during ion implantation. The upper layer is the region traversed by the implanted ions, with somewhat compromised properties due to the impact damage. However, the electrical, thermal, and optical properties of this surface layer are significantly less affected by the ion implantation process than the implanted layer, where the maximum damage occurs.

The purpose of this investigation is to present a three-layer model for a quantitative understanding of the PCR response from ion-implanted semiconductors. The dependence

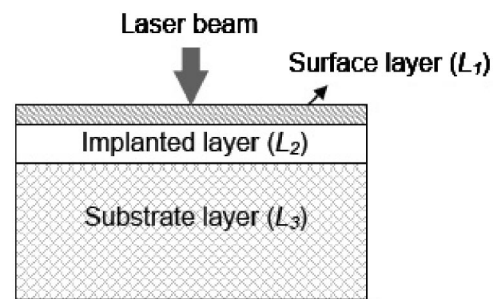


FIG. 1. Schematic diagram of the proposed three-layer structure of an ion-implanted silicon wafer.

of the PCR signal on the ion implantation dose is theoretically calculated and compared to experimental results. These results provide a basis for the development of PCR as an industrially competitive alternative to existing diagnostic techniques for semiconductor ion implantation process control.

II. THEORETICAL MODEL

The proposed structure of an ion-implanted semiconductor wafer is schematically presented in Fig. 1. A three-layer structure is assumed: a surface layer, an ion-implanted layer, and a substrate layer. The surface layer represents a region traversed by the implanted ions. The ions do not reside within this region. The thickness of this upper layer depends on the implantation species and energy and is usually in the range of 0–100 nm when the energy is not too high. The second region lies within 10–500 nm below the surface of the wafer and represents the implanted layer where damage is maximum. The thickness of this implanted layer depends on both the implantation energy and the implantation dose. For a given species, the thickness is mainly controlled by the implantation energy. For a given energy the thickness increases with increasing implantation dose. The third region is the remaining wafer and features transport and optical properties similar to the intact bulk wafer. The thicknesses of the three layers are denoted as L_1 , L_2 , and L_3 , respectively.

Since the actual damage profile in the substrate material is a continuously inhomogeneous region of compromised integrity above a crystalline substrate rather than regions with distinct boundaries, the optical and electrical properties, as well as the thickness, of the second layer in the assumed model represent weighted averages over the region affected by implantation. When the thickness of the damaged layer is small relative to the ac carrier diffusion length in the material the actual inhomogeneous layer can be expected to have effects on the carrier density wave, and consequently the PCR signal, similar to that of a discrete homogeneous damaged layer with transport properties that are a weighted average of the actual property profile and the assumed layer thickness.²¹ Similarly, when the thickness of the damaged region is small relative to the optical absorption depth of the excitation source the influence of the actual damage profile on the optical intensity as a function of the depth can be expected to be similar to that of a homogeneous layer with optical properties determined by some average of the actual optical prop-

erty profile and the assumed layer thickness. As the characteristic length of the optical or electronic field in the material becomes commensurate with the depth of the actual damage profile the treatment of the damaged region as a discrete layer becomes less appropriate and the model less reliable.

The PCR detection geometry is the same as that for PTR of semiconductors.^{23–25} The excitation beam is assumed to be Gaussian with a $(1/e)$ -radius equal to a . The beam is modulated with an angular frequency ω ($\omega = 2\pi f$) and focused onto the ion-implanted side of a laterally semi-infinite semiconductor wafer. In PCR measurements, the thermal infrared (Planck-mediated) emissions are filtered out and only infrared (IR) emissions from the free-carrier wave component are detected by an appropriate IR detector and spectrally matched filter combination.¹² In what follows we consider the specific case of a p -type Si wafer, although it is obvious that the theoretical treatment is quite generally applicable to Si and other semiconductor materials.

The optically injected carrier densities in the three layers are calculated from the following carrier transport equations:

$$\nabla^2 N_1(r, z, \omega) - \sigma_1^2 N_1(r, z, \omega) = -\frac{G_1(r, z, \omega)}{D_1}, \quad (1)$$

$$\nabla^2 N_2(r, z, \omega) - \sigma_2^2 N_2(r, z, \omega) = -\frac{G_2(r, z, \omega)}{D_2}, \quad (2)$$

$$\nabla^2 N_3(r, z, \omega) - \sigma_3^2 N_3(r, z, \omega) = -\frac{G_3(r, z, \omega)}{D_3}, \quad (3)$$

with the following boundary conditions at the front surface ($z=0$):

$$D_1 \frac{dN_1(r, z=0, \omega)}{dz} = s_1 N_1(r, z=0, \omega) \quad (4)$$

at the interface between the first and second layers ($z=L_1$)

$$N_1(r, z=L_1, \omega) = N_2(r, z=L_1, \omega), \quad (5)$$

$$D_1 \frac{dN_1(r, z=L_1, \omega)}{dz} = D_2 \frac{dN_2(r, z=L_1, \omega)}{dz} - s_2 N_2(r, z=L_1, \omega), \quad (6)$$

at the interface between the second and substrate layers ($z=L_1+L_2$)

$$N_2(r, z=L_1+L_2, \omega) = N_3(r, z=L_1+L_2, \omega), \quad (7)$$

$$D_2 \frac{dN_2(r, z=L_1+L_2, \omega)}{dz} = D_3 \frac{dN_3(r, z=L_1+L_2, \omega)}{dz} - s_3 N_3(r, z=L_1+L_2, \omega), \quad (8)$$

and at the rear surface ($z=L_1+L_2+L_3$)

$$D_3 \frac{dN_3(r, z=L_1+L_2+L_3, \omega)}{dz} = -s_4 N_3(r, z=L_1+L_2+L_3, \omega). \quad (9)$$

Where

$$\sigma_n^2 = \frac{1 + i\omega\tau_n}{D_n\tau_n} \quad (n=1,2,3), \quad (10)$$

$$G_1(r, z, \omega) = \frac{\alpha_1(1-R_1)P\eta}{\pi a^2 h\nu} \exp\left(-\frac{r^2}{a^2} - \alpha_1 z\right); \quad (11)$$

$$G_2(r, z, \omega) = \frac{\alpha_2(1-R_1)(1-R_2)P\eta}{\pi a^2 h\nu} \times \exp\left(-\frac{r^2}{a^2} - \alpha_1 L_1 - \alpha_2(z-L_1)\right); \quad (12)$$

$$G_3(r, z, \omega) = \frac{\alpha_3(1-R_1)(1-R_2)(1-R_3)P\eta}{\pi a^2 h\nu} \times \exp\left(-\frac{r^2}{a^2} - \alpha_1 L_1 - \alpha_2 L_2 - \alpha_3(z-L_1-L_2)\right). \quad (13)$$

Here D_n and τ_n ($n=1, 2, 3$) are the minority (electron) carrier diffusion coefficient and lifetime of the surface layer, implanted layer, and substrate layer, respectively. α_1 , α_2 , and α_3 are their absorption coefficients, respectively. s_1 and s_4 are the front and rear surface recombination velocities of the wafer, and s_2 and s_3 are the effective interface recombination velocities at the first and second interfaces, respectively. R_1 is the reflectivity of the front surface and R_2 and R_3 are the effective reflectivities at the two interfaces, respectively. P and $h\nu$ are the power and the photon energy of the incident laser beam. η is the quantum yield, which is the optical-to-electrical energy conversion efficiency.

The solutions to the transport Eqs. (1)–(3) together with the boundary conditions (4)–(9) can be easily obtained by using the (Hankel) integral transform method and are expressed as follows:

$$N_1(r, z, \omega) = \int_0^\infty \delta d \delta J_0(\delta r) [A_1 \exp(-\beta_1 z) + B_1 \exp(\beta_1 z) + E_1 \exp(-\alpha_1 z)], \quad (14)$$

$$N_2(r, z, \omega) = \int_0^\infty \delta d \delta J_0(\delta r) \{A_2 \exp[-\beta_2(z-L_1)] + B_2 \exp[\beta_2(z-L_1)] + E_2 \exp[-\alpha_2(z-L_1)]\}, \quad (15)$$

$$N_3(r, z, \omega) = \int_0^\infty \delta d \delta J_0(\delta r) \{A_3 \exp[-\beta_3(z-L_1-L_2)] + B_3 \exp[\beta_3(z-L_1-L_2)] + E_3 \exp[-\alpha_3(z-L_1-L_2)]\}. \quad (16)$$

The various symbols are defined in the Appendix.

The PCR signal is obtained by integrating the carrier density over the thickness of the whole wafer, which takes into account deep-lying bulk radiation emission from photo-generated and diffused carriers.²⁶ That is

TABLE I. Transport and optical properties of crystalline and amorphous silicon.

Parameter	Unit	Crystalline Si	Amorphous Si
Carrier lifetime ^a	μs	10	0.001
Carrier diffusion coefficient	cm^2/s	20 ^b	0.1 ^c
Absorption coefficient at 830 nm ^d	m^{-1}	6.6×10^4	2.0×10^6

^aReference 18.

^bAmbipolar diffusion coefficient.

^cReference 31.

^dReference 32.

$$S_{\text{PCR}}(r, \omega) = C_1 \left[\int_0^{L_1} N_1(r, z, \omega) dz + \int_{L_1}^{L_1+L_2} N_2(r, z, \omega) dz + \int_{L_1+L_2}^{L_1+L_2+L_3} N_3(r, z, \omega) dz \right]. \quad (17)$$

The result is

$$S_{\text{PCR}}(r, \omega) = C_1 \int_0^\infty \tilde{F}(\delta, \omega) \delta d J_0(\delta r), \quad (18)$$

with C_1 being a proportionality constant, and

$$\begin{aligned} \tilde{F}(\delta, \omega) = & \frac{1 - \exp(-\beta_1 L_1)}{\beta_1} [A_1 + B_1 \exp(\beta_1 L_1)] \\ & + \frac{E_1}{\alpha_1} [1 - \exp(-\alpha_1 L_1)] + \frac{1 - \exp(-\beta_2 L_2)}{\beta_2} \\ & \times [A_2 + B_2 \exp(\beta_2 L_2)] + \frac{E_2}{\alpha_2} [1 - \exp(-\alpha_2 L_2)] \\ & + \frac{1 - \exp(-\beta_3 L_3)}{\beta_3} [A_3 + B_3 \exp(\beta_3 L_3)] \\ & + \frac{E_3}{\alpha_3} [1 - \exp(-\alpha_3 L_3)]. \end{aligned} \quad (19)$$

The collection efficiency of the IR detector can be taken into account by integrating the resulting expression over the effective aperture (or the area) of the detector, assuming a circular shape with a radius of w ²³

$$\begin{aligned} S_{\text{PCR}}(\omega) = & 2\pi \int_0^w S_{\text{PCR}}(r, \omega) r dr \\ = & C_2 \int_0^\infty \tilde{F}(\delta, \omega) J_1(\delta w) d\delta. \end{aligned} \quad (20)$$

Here C_2 is another proportionality factor which is independent of the transport properties of the wafer and the modulation frequency. Equation (20) represents the PCR signal detected by the IR detector.

Next, we will discuss the dependence of the PCR amplitude on ion implantation dose (d) by calculating the influence of the minority carrier lifetime (τ_2), diffusion coefficient (D_2), optical absorption coefficient (α_2), and thickness (L_2) of the implanted layer, as well as the front surface recombination velocity (s_1) on the PCR signal, as

these parameters are strongly affected by the lattice damage caused by ion implantation. For simplicity, the transport (τ , D) and optical (α) properties of the surface layer and substrate are assumed to be dose-independent.

To calculate the dependence of the PCR signal on implantation dose, the relationships between parameters τ_2 , D_2 , α_2 , L_2 , and s_1 and implantation dose d have to be established first. For τ_2 , D_2 , α_2 , these relationships are based on their correlation to damage introduced to the lattice by ion implantation. With increasing implantation dose, increasing crystalline damage results in a decrease of τ_2 and D_2 , as well as an increase of α_2 . The quantitative relationships between τ_2 , D_2 , α_2 , and d are established by using the effective medium approximation,^{27,28} similar to that used in Ref. 18. The damage rate D is assumed to follow a simple saturation law²⁹

$$D = 1 - \exp(-d/d_0), \quad (21)$$

where d_0 is an experimental dose determined by implantation parameters such as species and energy. $D=0$ means the implanted region is in perfect crystalline phase while $D=1$ represents a total damage and a change of the crystalline lattice to an amorphous phase (for optical properties). Usually for electrical transport parameters the d_0 value is lower than that for the optical properties,^{19,30} which means that the electrical damage occurs well before the optical damage. In the calculations, we assume one d_0 value for τ_2 and D_2 and another different value for α_2 . The values of τ_2 , D_2 , α_2 are those of crystalline silicon when $D=0$ and are those of amorphous silicon when $D=1$. The transport and optical properties of crystalline and amorphous silicon are listed in Table I.

The thickness of the implanted layer increases with increasing implantation dose since the damaged region widens with increasing dose.³³⁻³⁵ The dose-dependent thickness can be approximately expressed as³⁵

$$l_2 = l_{20} + \Delta l_2 \times \log_{10}(d/d_{\text{low}}). \quad (22)$$

Here, l_{20} is the thickness of the implanted layer at the low dose end (d_{low}). Δl_2 is the increase in thickness over one order of magnitude increase in dose. Both l_{20} and Δl_2 are functions of implantation species and energy.

There have been reports³⁶⁻³⁸ that the front surface recombination velocity changes with implantation dose. However, no reliable quantitative information could be found in the literature. Our measurements³⁹ on ion-implanted silicon wafers indicate that the front surface recombination velocity increases rapidly with increasing dose at the low dose end

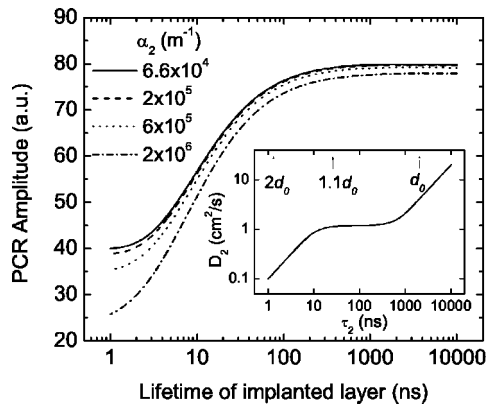


FIG. 2. PCR amplitude as a function of the carrier lifetime of the implanted layer. The modulation frequency is assumed to be 1 kHz. Inset shows how the carrier diffusion coefficient varies with lifetime, assuming both are determined by the transport properties of crystalline and amorphous silicon and the damage rate, following the effective medium approximation. The corresponding doses are indicated in the inset by arrows. d_0 is the dose factor for the electrical damage.

and saturates gradually from intermediate to high doses. Based on this observation, the front surface recombination velocity is empirically assumed to follow:

$$s_1 = s_{10}(d/d_{\text{low}})^x, \quad (23)$$

where s_{10} is the recombination velocity at the low dose range represented by d_{low} . x is an empirical exponent between 0 and 1. Other parameter values assumed in the calculations include: $\tau_1 = 1 \mu\text{s}$, $D_1 = 2 \text{ cm}^2/\text{s}$, $\alpha_1 = 6.6 \times 10^4 \text{ m}^{-1}$, $L_1 = 10 \text{ nm}$; and $\tau_3 = 10 \mu\text{s}$, $D_3 = 20 \text{ cm}^2/\text{s}$, $\alpha_3 = 6.6 \times 10^4 \text{ m}^{-1}$, $L_3 = 670 \mu\text{m}$; $s_4 = 1 \times 10^4 \text{ cm/s}$. In addition, recombination at the two interfaces is neglected ($s_2 = 0$, $s_3 = 0$) because in reality there are no sharp boundaries to contribute to enhanced recombination there. For the experimental parameters, the radius of the pump laser beam was measured by a pinhole scan and was found to be $25 \mu\text{m}$. The effective size of the detector was determined to be $55 \mu\text{m}$.

III. SIMULATIONS, EXPERIMENTAL RESULTS, AND DISCUSSION

To investigate the dependence of the PCR signal on implantation dose, the influence of each individual parameter (τ_2 , D_2 , α_2 , L_2 , and s_1) affected by ion implantation is calculated first. Figure 2 shows the dependence of the PCR amplitude on the carrier lifetime of the implanted layer. The PCR phase is not used in the simulations because it is insensitive to the changes of the electrical and optical properties of the implanted layer in the low frequency range used in the experiments ($< 100 \text{ kHz}$).¹⁴ The carrier diffusion coefficient of the implanted layer was assumed to change along with the lifetime based on the damage rate D and the effective medium approximation, as shown in the inset. The thickness of the layer was assumed to be $0.3 \mu\text{m}$, the front surface recombination velocity was assumed to be 1000 cm/s , and the modulation frequency was assumed to be 1 kHz . When the dose is lower than or very close to the dose factor (d_0) for the electrical damage the ion-implantation induced damage is low (inset in Fig. 2), the somewhat reduced carrier lifetime

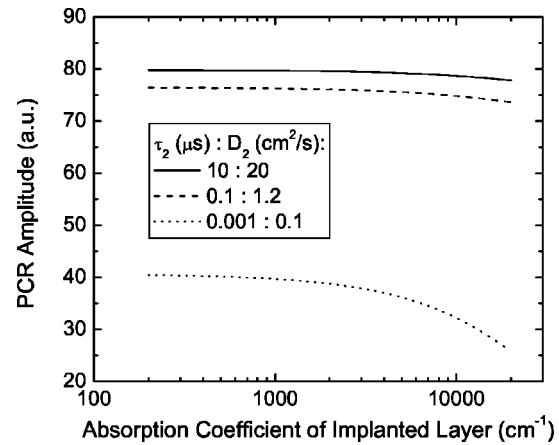


FIG. 3. PCR amplitude as a function of the absorption coefficient of the implanted layer at various electrical damage rates. The modulation frequency is 1 kHz .

and diffusion coefficient of the implanted layer have negligible effect on the PCR amplitude. As the implantation-induced damage increases, the carrier lifetime and diffusion coefficient decrease rapidly. As the lifetime becomes less than approximately $0.2 \mu\text{s}$, the PCR amplitude starts to decrease rapidly with decreasing carrier lifetime until saturation-like behavior emerges at the low lifetime (high damage) end. This saturation behavior is caused by the partial compensation due to the simultaneous decrease of the carrier diffusion coefficient. While the PCR amplitude decreases with decreasing carrier lifetime alone, it increases with decreasing diffusion coefficient, if the lifetime is kept unchanged since fewer carriers are leaving the field of view of the detector. As the optical absorption coefficient increases, the magnitude of decline of the PCR amplitude increases because a proportionally greater number of free carriers are generated within the vicinity of the damaged region, thus lowering the effective lifetime and hence the PCR amplitude. While α increases, the number of free photoexcited carriers in the bulk decreases, a fact that further accelerates the decrease of the PCR amplitude. The reduced carrier lifetime dominates the effect of the decreased diffusion coefficient when the absorption coefficient is high, resulting in a less saturated behavior at the high damage end.

Ion implantation also has an influence on the optical absorption coefficient of the implanted layer. When there is no lattice damage, the optical property of a silicon wafer is controlled by the crystalline phase. As implantation damage increases in the implanted layer, the absorption coefficient increases accordingly. The absorption coefficient saturates to that of amorphous silicon when the crystalline lattice of the implanted layer changes to a totally amorphous phase at the high dose end. The absorption coefficient of amorphous silicon at the pump laser wavelength (830 nm) is more than one order of magnitude (approximately 30 times) higher than that of the crystalline silicon (See Table I). Figure 3 presents the dependence of the PCR amplitude on the absorption coefficient at various electrical damage levels. The thickness of the implanted layer was assumed to be $0.3 \mu\text{m}$, the front surface recombination velocity was assumed to be 1000 cm/s , and

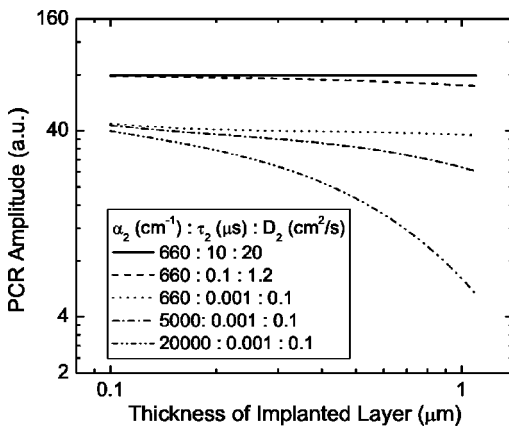


FIG. 4. PCR amplitude as a function of the thickness of the implanted layer at various electrical and optical damage rates. The modulation frequency is 1 kHz.

the modulation frequency was assumed to be 1 kHz. The effect of the absorption coefficient on the PCR amplitude depends largely on the electrical damage level which in turn determines the carrier lifetime and diffusion coefficient of the implanted layer. The influence of an increasing absorption coefficient on the PCR amplitude is significant only when strong electrical damage is present. In fact, this is always the case as ion-implantation-induced electrical damage occurs well before the optical damage appears. In this case, the PCR amplitude decreases with an increasing absorption coefficient. In conclusion, the higher the electrical damage level, the more rapidly the PCR amplitude decreases with increasing absorption coefficient.

The thickness of the implanted layer increases with the increasing implantation dose as the crystalline damage widens into the substrate. This increase in the thickness may also cause the PCR amplitude to drop, depending on the electrical and optical damage levels of the implanted layer. Figure 4 presents the dependence of the PCR amplitude on the thickness of the implanted layer at different electrical and optical damage levels. The front surface recombination velocity was assumed to be 1000 cm/s and the modulation frequency was assumed to be 1 kHz. With only electrical damage but no optical damage, the PCR amplitude decreases only slightly with increasing thickness since only those carriers generated in the substrate region very close to the damaged region can diffuse from the substrate to the damaged region and be trapped there. However, when the optical damage also appears, the decline of PCR amplitude due to the increasing thickness of the damaged layer accelerates with an increasing absorption coefficient as the implanted layer becomes less optically transparent and attenuates more of the incident laser power, resulting in a reduced photogenerated carrier density in the bulk region.

The dependence of the PCR amplitude on the front surface recombination velocity at various electrical and optical damage levels is presented in Fig. 5. The thickness of the implanted layer was assumed to be 0.3 μm and the modulation frequency was assumed to be 1 kHz. The simulations show that the front surface recombination velocity affects the PCR amplitude only when there is no electrical damage level

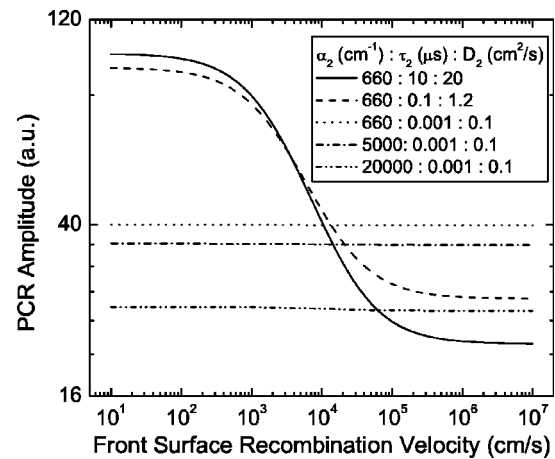


FIG. 5. PCR amplitude as a function of the front surface recombination velocity at various electrical and optical damage rates. The modulation frequency is 1 kHz.

or when damage is low. With no electrical damage, the PCR amplitude is insensitive to the surface recombination velocity at the low end because the overall effect of a low surface recombination to the PCR signal is still negligible. As the front surface recombination velocity further increases, the PCR amplitude decreases rapidly in the 1000–1 × 10⁵ cm/s velocity range, then becomes saturated at the high recombination velocity end. As the electrical damage increases, the effect of the surface recombination on the PCR signal becomes less significant. This is because the electrical damage reduces both the carrier lifetime and diffusion coefficient of the implanted layer, resulting in a shorter diffusion length (the dc diffusion length of the implanted layer is defined as $\mu_{2dc} = \sqrt{D_2 \tau_2}$) in the implanted layer. The implanted layer therefore acts as an electrical barrier which blocks carrier diffusion from the substrate region to the surface region where surface recombination takes place. With maximum electrical damage, the dc diffusion length (0.1 μm) is shorter than the thickness of the implanted layer. The implanted layer becomes electrically thick and the PCR signal becomes independent of the surface recombination velocity, regardless of the absorption coefficient.

Taking into account the effects of ion implantation on all individual parameters discussed above, Fig. 6 shows the PCR amplitude as a function of ion implantation dose, with and without changing the thickness of the implanted layer and front surface recombination velocity as functions of dose. In the calculations, the modulation frequency was assumed to be 1 kHz. The experimental dose factors d_0 for the transport and optical properties were assumed to be 1 × 10¹¹ and 1 × 10¹⁴ cm⁻², respectively. l_{20} , Δl_2 , s_{10} , x , and d_{low} were assumed to be 0.2 μm, 0.06 μm, 1000 cm/s, 0.75, and 1 × 10¹⁰ cm⁻², respectively. At high dose, s_1 was assumed to be saturated at 1 × 10⁶ cm/s. Inspection of Fig. 6 indicates that the PCR signal dependence on the implantation dose can be broken into four regions with the transition across each region defined by the electrical (transport) and optical damage dose factor d_0 . In region I the PCR amplitude decreases rapidly with dose due to a combined effect of increasing surface recombination and decreasing carrier life-

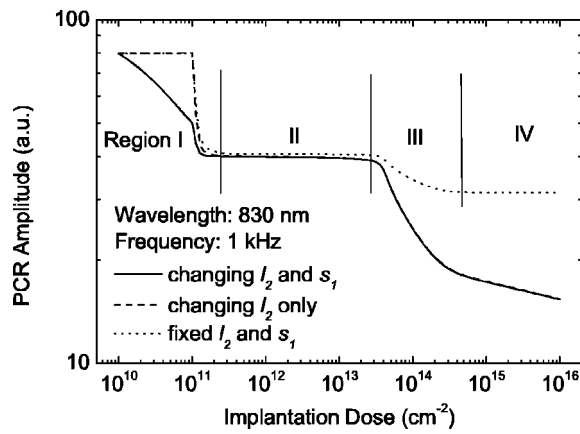


FIG. 6. Theoretical PCR amplitude as a function of implantation dose. The modulation frequency is 1 kHz. Solid line: both the thickness of the implanted layer and the front surface recombination velocity were assumed to be a function of dose; dashed line: the front surface recombination velocity was assumed to be 1000 cm/s, independent of dose; dotted line: the thickness of the implanted layer and the front surface recombination velocity were both assumed to be independent of dose.

time and diffusion coefficient in the implanted layer. In the second region the electrical damage is totally saturated and optical damage is not yet present. In this region the PCR amplitude decreases only slightly due to the increasing size of the electrically damaged region with dose. If the thickness of the implanted layer was assumed to be independent of dose, the PCR amplitude would be totally independent of implantation dose in this region (see dotted line in Fig. 6). In the third region the optical damage begins to appear with an increasing dose, the PCR amplitude decreases and eventually becomes much less sensitive to increasing dose when the optical damage is totally saturated since then only the increasing thickness contributes to the decline of the PCR amplitude. In region IV, the sensitivity of the PCR signal to dose is again low as both the electrical and optical types of damage in this region are saturated. The slight decrease of PCR amplitude with dose is the result of a widening damaged region, as is the case in region II. Nevertheless, the dose sensitivity in region IV is higher than that in region II as both electrical and optical types of damage are present in region IV. From Fig. 6, it is also clear that the increasing surface recombination velocity with dose affects the PCR signal only in region I. If the surface recombination velocity were assumed to be constant, the electrical damage would have caused a sharp decline of PCR amplitude in a very narrow dose range.

Experiments with several industrial Si wafers were performed to verify the theoretical predictions presented above. The experimental setup has been described in detail elsewhere.^{12,13} A tunable Ti: sapphire laser pumped by a 10 W 532 nm laser was used as the excitation source. The laser was operated at 830 nm wavelength and the power of the beam was 22.8 mW. The laser beam was focused onto the sample surface and the radius of the beam at the surface was measured to be approximately 25 μm . The infrared emission from the sample was collected and focused through a pair of reflective objectives onto an InGaAs detector, preamplifier, and optical cut-on filter assembly. The effective radius of the

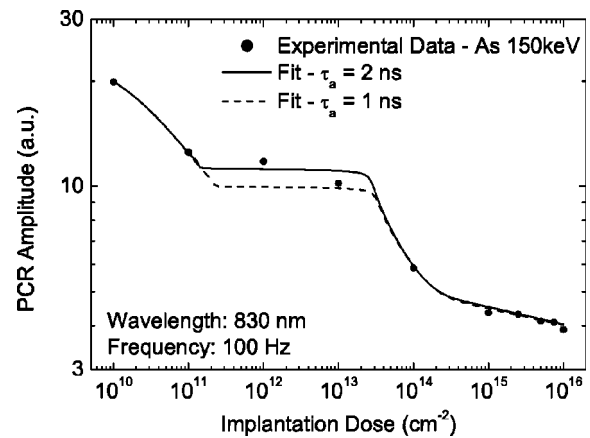


FIG. 7. Experimental dependence of PCR amplitude on the implantation dose with theoretical fits. The modulation frequency was 100 Hz. The silicon wafers were As^+ implanted at 150 keV energy. The carrier lifetime of amorphous silicon was assumed to be 2 ns (solid line) and 1 ns (dashed line), respectively.

detector was estimated to be 55 μm . The spectral response range of the detector optics was 0.8–1.8 μm . The spectrally matched filter further served to block any leakage of the excitation source. The samples used in the experiments were (100) oriented p -type silicon wafers, 10–20 Ωcm , implanted with $^{75}\text{As}^+$ at an energy of 150 keV. The thicknesses of these wafers were $675 \pm 20\ \mu\text{m}$. The wafers were implanted at room temperature at an angle of 7° to suppress channeling with doses from 1×10^{10} to $1 \times 10^{16}\ \text{cm}^{-2}$.

The experimental results are presented in Fig. 7 together with two theoretical fits, with the carrier lifetime (τ_a) of amorphous silicon assumed to be 1 and 2 ns, respectively. When τ_a is assumed to be 2 ns, a good fit between theoretical calculation and experimental data is obtained when the dose factors for electrical damage (d_{01}) and optical damage (d_{02}) are assumed to be 1.2×10^{11} and $7 \times 10^{13}\ \text{cm}^{-2}$, respectively, and the thickness of the implanted layer is assumed to be $l_2 = 0.28 + 0.06 \log_{10}(d/1 \times 10^{10})\ \mu\text{m}$. When τ_a was taken as 1 ns, a good fit was obtained when the other parameters were taken as $d_{01} = 2 \times 10^{11}\ \text{cm}^{-2}$, $d_{02} = 8 \times 10^{13}\ \text{cm}^{-2}$, and $l_2 = 0.2 + 0.056 \log_{10}(d/1 \times 10^{10})\ \mu\text{m}$. In both cases the diffusion coefficient of amorphous silicon was fixed to be 0.1 cm^2/s , the reported literature value,¹⁸ and the front surface recombination velocity was assumed to follow $s_1 = 1000 \times (d/1 \times 10^{10})^{0.75}\ \text{cm/s}$. In general, the agreement between the experimental data and theoretical fits is quite good, taking into account the fact that many of the parameter values are not readily available in the literature. The fitted dose factor for the optical damage is close to that reported by Cortot and Ged.²⁹ The good agreement between the experimental and theoretical data in the intermediate to high dose region indicates that the optical damage model appropriately describes the PCR signal behavior in this dose range, as the optical properties of implanted silicon wafers have been widely measured^{29,30,40} and the dependence of the absorption coefficient on implantation dose is well established. On the other hand, the discrepancy in the intermediate dose region may be due to an over-simplification of the relationship between the electrical damage and the implantation dose as-

sumed in Eq. (21). Even though reported experimental observations³⁰ confirmed that the electrical (transport) properties of implanted wafers are more sensitive to the lattice damage caused by ion implantation than the optical properties, no data are currently available to establish a convincing quantitative dependence of the electrical damage on implantation dose. Our experimental results indicate the dependence of the electrical damage rate on dose may be less sharp than that assumed by the saturation law.

Both experimental data and theoretical predictions indicate that the PCR amplitude is a monotonic function of the implantation dose over the entire dose range of technical interest. This monotonic behavior is an advantage over photothermal techniques, such as PMR, which exhibit nonmonotonic dependence.^{18,19} It is of considerable technical importance for the development of techniques and instrumentation to monitor ion-implantation dose. In addition, the high sensitivity of PCR amplitude to dose at both low and high dose ends makes it a highly attractive candidate for dose monitoring in industrial environments as these dose ranges are of increasing technical importance with, e.g., complementary metal-oxide semiconductor technologies, ultra-shallow implants, and epitaxial thin layers, to name a few.

IV. CONCLUSIONS

A three-dimensional three-layer model has been developed to quantitatively describe the PCR response of ion-implanted semiconductors. The dependence of the PCR signal on the ion-implantation dose has been theoretically calculated and compared to experimental results. Good agreement between experimental data and theoretical calculations has been obtained. The predicted theoretical results and the experimental data both confirmed the monotonic dependence of PCR signal on the ion implantation dose. This monotonic behavior makes the PCR technique a potentially significant candidate for industrial ion implantation process control in semiconductor manufacturing.

ACKNOWLEDGMENTS

The financial support of Materials and Manufacturing Ontario (MMO) through a Collaborative Contract to A.M. and of the Natural Science and Engineering Council of Canada (NSERC) is gratefully acknowledged.

APPENDIX

Symbol definitions appearing in Eqs. (14)–(16)

$$\beta_n^2 = \delta^2 + \sigma_n^2, \quad (n = 1, 2, 3) \quad (A1)$$

$$E_1 = \frac{\alpha_1(1-R_1)\eta P}{2\pi h\nu D_1} \cdot \frac{\exp(-\delta^2 a^2/4)}{\beta_1^2 - \alpha_1^2}, \quad (A2)$$

$$E_2 = \frac{\alpha_2(1-R_1)(1-R_2)\eta P}{2\pi h\nu D_2} \cdot \frac{\exp(-\delta^2 a^2/4 - \alpha_1 L_1)}{\beta_2^2 - \alpha_2^2}, \quad (A3)$$

$$E_3 = \frac{\alpha_3(1-R_1)(1-R_2)(1-R_3)\eta P}{2\pi h\nu D_3} \cdot \frac{\exp(-\delta^2 a^2/4 - \alpha_1 L_1 - \alpha_2 L_2)}{\beta_3^2 - \alpha_3^2}, \quad (A4)$$

$$A_1 = \frac{1}{H} \left\{ - \left[\frac{b_1}{a_1} (a_2 + p_2 g_1) \exp(\beta_1 L_1) - (b_2 - p_2 g_1) \times \exp(-\alpha_1 L_1) \right] E_1 + [p_2 g_1 (1 + \gamma_2) + (g_1 \gamma_2 - h_2)] E_2 + \frac{2g_1 \gamma_3}{1 + \gamma_1} E_3 \right\}, \quad (A5)$$

$$B_1 = \frac{1}{a_1 H} \left\{ - [b_1 (1 - p_2 g_1) \exp(-\beta_1 L_1) - (b_2 - p_2 g_1) \times \exp(-\alpha_1 L_1)] E_1 + [p_2 g_1 (1 + \gamma_2) + (g_1 \gamma_2 - h_2)] E_2 + \frac{2g_1 \gamma_3}{1 + \gamma_1} E_3 \right\}, \quad (A6)$$

$$H = \frac{1}{a_1} (a_2 + p_2 g_1) \exp(\beta_1 L_1) - (1 - p_2 g_1) \exp(-\beta_1 L_1); \quad (A7)$$

$$A_2 = \frac{1}{2g_1} [(1 + g_1) A_1 \exp(-\beta_1 L_1) + (g_1 - a_2) B_1 \times \exp(\beta_1 L_1) + (g_1 + b_2) E_1 \exp(-\alpha_1 L_1) - (g_1 + h_1) E_2], \quad (A8)$$

$$B_2 = \gamma_1 A_2 + \gamma_2 E_2 + \gamma_3 E_3; \quad (A9)$$

$$A_3 = \frac{1}{2g_2} [(1 + g_2) A_2 \exp(-\beta_2 L_2) + (g_2 - a_3) B_2 \times \exp(\beta_2 L_2) + (g_2 + b_3) E_2 \exp(-\alpha_2 L_2) - (g_2 + h_2) E_3] \quad (A10)$$

$$B_3 = \mu A_3 + \gamma E_3; \quad (A11)$$

with

$$a_1 = \frac{D_1 \beta_1 - s_1}{D_1 \beta_1 + s_1}, \quad (A12)$$

$$b_1 = \frac{D_1 \alpha_1 + s_1}{D_1 \beta_1 + s_1}, \quad (A13)$$

$$a_2 = \frac{D_1 \beta_1 + s_2}{D_1 \beta_1 - s_2}, \quad (A14)$$

$$b_2 = \frac{D_1 \alpha_1 - s_2}{D_1 \beta_1 - s_2}, \quad (A15)$$

$$a_3 = \frac{D_2 \beta_2 + s_3}{D_2 \beta_2 - s_3}, \quad (A16)$$

$$b_3 = \frac{D_2 \alpha_2 - s_3}{D_2 \beta_2 - s_3}, \quad (A17)$$

$$a_4 = \frac{D_3\beta_3 + s_4}{D_3\beta_3 - s_4}, \quad (\text{A18})$$

$$b_4 = \frac{D_3\alpha_3 - s_4}{D_3\beta_3 - s_4}, \quad (\text{A19})$$

$$g_1 = \frac{D_2\beta_2}{D_1\beta_1 - s_2}, \quad (\text{A20})$$

$$g_2 = \frac{D_3\beta_3}{D_2\beta_2 - s_3}, \quad (\text{A21})$$

$$h_1 = \frac{D_2\alpha_2}{D_1\beta_1 - s_2}, \quad (\text{A22})$$

$$h_2 = \frac{D_3\alpha_3}{D_2\beta_2 - s_3}, \quad (\text{A23})$$

$$\mu = \frac{1}{a_4} \exp(-2\beta_3 L_3), \quad (\text{A24})$$

$$\gamma = \frac{b_4}{a_4} \exp(-\beta_3 L_3 - \alpha_3 L_3), \quad (\text{A25})$$

$$p_1 = \frac{1 - \mu}{1 + \mu}, \quad (\text{A26})$$

$$\gamma_1 = \frac{1 - p_1 g_2}{a_3 + p_1 g_2} \exp(-2\beta_2 L_2), \quad (\text{A27})$$

$$\gamma_2 = \frac{b_3 - p_1 g_2}{a_3 + p_1 g_2} \exp(-\beta_2 L_2 - \alpha_2 L_2), \quad (\text{A28})$$

$$\gamma_3 = \frac{p_1 g_2 (1 + \gamma) + g_2 \gamma - h_2}{a_3 + p_1 g_2} \exp(-\beta_2 L_2), \quad (\text{A29})$$

$$p_2 = \frac{1 - \gamma_1}{1 + \gamma_1}. \quad (\text{A30})$$

¹E. Chason, S. T. Picraux, J. M. Poate, J. O. Borland, M. I. Current, T. Diaz de la Rubia, D. J. Eaglesham, O. W. Holland, M. E. Law, C. W. Magee, J. W. Mayer, J. Melngailis, and A. F. Tasch, *J. Appl. Phys.* **81**, 6513 (1997).

²T. Clarysse, W. Vandervorst, E. J. H. Collart, and A. J. Murrell, *J. Electrochem. Soc.* **147**, 3569 (2000).

³D. K. Schroder, *Semiconductor Material and Device Characterization 2nd ed.* (Wiley, New York, 1998), Chap. 1.

⁴J. P. Esteves and M. J. Rendon, *AIP Conf. Proc.* **449**, 369 (1998).

⁵W. L. Smith, A. Rosencwaig, and D. L. Willenborg, *Appl. Phys. Lett.* **47**, 584 (1985).

⁶A. Rosencwaig, J. Opsal, W. L. Smith, and D. Willenborg, *Appl. Phys. Lett.* **46**, 1013 (1985).

⁷C. Christofides, I. A. Vitkin, and A. Mandelis, *J. Appl. Phys.* **67**, 2815 (1990).

⁸A. Vitkin, C. Christofides, and A. Mandelis, *J. Appl. Phys.* **67**, 2822 (1990).

⁹A. Othonos, C. Christofides, and A. Mandelis, *Appl. Phys. Lett.* **69**, 821 (1996).

¹⁰A. Salmick, A. Mandelis, F. Funak, and C. Jean, *Appl. Phys. Lett.* **71**, 1531 (1997).

¹¹A. Mandelis, *Solid-State Electron.* **41**, 591 (1997).

¹²A. Mandelis, J. Batista, and D. Shaughnessy, *Phys. Rev. B* **67**, 205 208 (2003).

¹³J. Batista, A. Mandelis, and D. Shaughnessy, *Appl. Phys. Lett.* **82**, 4077 (2003).

¹⁴D. Shaughnessy, B. Li, A. Mandelis, and J. Batista, *Appl. Phys. Lett.* (Submitted).

¹⁵S. Wurm, P. Alpern, D. Savignac, and R. Kakoschke, *Appl. Phys. A: Solids Surf.* **47**, 147 (1988).

¹⁶C. Christofides, F. Diakonou, A. Seas, C. Christou, M. Nestoros, and A. Mandelis, *J. Appl. Phys.* **80**, 1713 (1996).

¹⁷M. Liu, M. B. Suddendorf, M. G. Somekh, and S. J. Sheard, *Semicond. Sci. Technol.* **8**, 1639 (1993).

¹⁸A. Salmick and J. Opsal, *J. Appl. Phys.* **91**, 2874 (2002).

¹⁹A. Salmick and J. Opsal, *Rev. Sci. Instrum.* **74**, 545 (2003).

²⁰M. Nestoros, Y. Karmiotis, and C. Christofides, *J. Appl. Phys.* **82**, 6220 (1997).

²¹A. Salmick and A. Mandelis, *J. Appl. Phys.* **80**, 5278 (1996).

²²A. Salmick, A. Mandelis, A. Othonos, and C. Christofides, in *Review of Progress in Quantitative Nondestructive Evaluation*, edited by D. O. Thompson and D. E. Chimenti (Plenum, New York, 1997) Vol. 16, pp. 371–378.

²³T. Ikari, A. Salmick, and A. Mandelis, *J. Appl. Phys.* **85**, 7392 (1999).

²⁴M. E. Rodriguez, A. Mandelis, G. Pan, J. A. Garcia, V. Gorodokin, and Y. Raskin, *J. Appl. Phys.* **87**, 8113 (2000).

²⁵D. Shaughnessy and A. Mandelis, *J. Appl. Phys.* **93**, 5244 (2003).

²⁶A. Mandelis, *Solid-State Electron.* **42**, 1 (1998).

²⁷G. Popescu and I. Boca, *Thin Solid Films* **233**, 207 (1993).

²⁸M. Fried, and Redei, *Thin Solid Films* **364**, 64 (2000).

²⁹J. P. Cortot and Ph. Ged, *Appl. Phys. Lett.* **41**, 93 (1982).

³⁰Ch. Wilbertz, K. L. Bhatia, W. Kraetschmer, and S. Kalbitzer, *Mater. Sci. Eng., B* **2**, 325 (1989).

³¹J. Opsal and A. Rosencwaig, *Appl. Phys. Lett.* **47**, 498 (1985).

³²*Handbook of Optical Constants of Solids*, edited by E. D. Palik, Vols. I and III (San Diego, Academic, 1998).

³³B. L. Crowder, R. S. Title, M. H. Brodsky, and G. D. Pettit, *Appl. Phys. Lett.* **16**, 205 (1970).

³⁴S. Prussin, D. I. Margolese, and R. N. Tauber, *J. Appl. Phys.* **57**, 180 (1985).

³⁵S. Prussin, D. I. Margolese, and R. N. Tauber, *J. Appl. Phys.* **54**, 2316 (1983).

³⁶T. Makino, M. Ichimura, H. Yoshida, E. Morita, and A. Usami, *Jpn. J. Appl. Phys., Part 1* **36**, 301 (1997).

³⁷A. Cuevas, P. A. Basore, G. Giroult-Matlakowski, and C. Dubois, *J. Appl. Phys.* **80**, 3370 (1996).

³⁸M. Nestoros, B. C. Forget, C. Christofides, and A. Seas, *Phys. Rev. B* **51**, 14 115 (1995).

³⁹B. Li, D. Shaughnessy, A. Mandelis, J. Batista, and J. Garcia (unpublished).

⁴⁰U. Zammit, K. N. Madhusoodanan, M. Marinelli, F. Scudieri, R. Pizzoferrato, and F. Mercuri, *Phys. Rev. B* **49**, 14 322 (1994).